Article

Numerical and Experimental Investigations of Composite Solar Walls Integrating Sensible or Latent Heat Thermal Storage

Enghok Leang, Pierre Tittelein, Laurent Zalewski * and Stéphane Lassue

Laboratoire de Génie Civil et géo-Environnement (LGCgE), ULR 4515, Univ. Artois, F-62400 Béthune, France; enghok.leang@univ-artois.fr (E.L.); pierre.tittelein@univ-artois.fr (P.T.); stephane.lassue@univ-artois.fr (S.L.)

* Correspondence: laurent.zalewski@univ-artois.fr

Abstract: This article studies a composite solar wall with latent storage (TES) designed to heat rooms inside buildings during the cold season. No numerical model of the composite solar wall is currently available in the *Dymola/Modelica* software library. The first objective of this work is to develop one such model. The article describes the elementary components, along with the equations that allow modeling the heat transfers and storage phenomena governing both the thermal behavior and performance of the solar wall. This model was built by assembling various existing basic elements from the software's "Building" library (e.g., models of heat transfer by convection, radiation and conduction) and then creating new elements, such as the storage element incorporating the phase change material (PCM). To validate this solar wall model, numerical results are compared to experimental data stemming from a small-scale composite solar wall manufactured in our laboratory, and the experimental set-up could be tested under real weather conditions. After verifying the level of confidence in the model, the energy performance of two solar walls, one with a conventional storage wall (sensible heat storage) the other containing a PCM (the same as in the experiment), are compared. The result indicates that the solar wall incorporating a PCM does not in this case release any more energy in the room to be heated.

Keywords: composite Trombe wall; phase change material; micro-encapsulated PCM

1. Introduction

To limit the energy consumption required to heat building space in winter, several strategies were explored, including the passive solar wall. Integrated into the building envelope, a passive solar wall has drawn researchers' attention in determining the potential benefit achieved from such a system. Previous work has focused on: Trombe-Michel systems yielding more air power entering the room during sunny hours [1]; passive solar air heating and natural ventilation via the buoyancy effect [2]; a ventilated Trombe wall as a passive solar heating and cooling retrofitting approach, serving to reduce the heating and cooling loads by 94% and 73% respectively [3]; the greenhouse effect with a passive Trombe wall providing higher temperature to the greenhouse air [4]; and a Trombe wall with direct gain generating the comfort of thermal heat [5]. Passive solar wall techniques, whether heating or cooling applications, can reduce annual energy consumption in the residential building sector, i.e.: the electrical consumption of a passive cooling wall containing PCM cubicles by 15% [6]; a solar heating system and air-water heat pump [7]; 35% offered by a passive solar agricultural greenhouse over a 2-year period [8]; passive cooling strategies to reduce the annual cooling energy consumption by up to 23.6% [9]; and a state-of-the-art report on possible methods relative to heating and cooling energy consumption [10]. This strategy started development decades ago, ever since its

first assessment by E.S. Morse in the 19th century. It was subsequently redesigned as an architectural element by F. Trombe and J. Michel [11], as frequently acknowledged in published papers on: Trombe wall, Trombe-Michel solar wall, or composite solar wall. In current research dedicated to energy and environmental contexts, passive solar wall techniques are more relevant than ever, leading to the development of various passive configurations, namely: (a) the classical Trombe wall: engineering techniques [12], theoretical and experimental investigations of heat transfer [13], comparison of the effects of air flow rate between the one-dimensional and two-dimensional models [14], and the numerical study of thermal performance [15]; (b) the PCM Trombe wall: clay bricks integrating PCM macro-capsules functioning as the storage wall [16], thermal performance of a PCM storage wall in temperate and hot climates [17], a simulation study of building walls using the collector-storage wall integrating PCMs [18], a summary of the investigation and analysis conducted on systems incorporating PCMs as storage elements [19], the heat storage wall of the studied building ventilation using black paraffin wax [20], and experimental investigations of PCM wall thermal performance improved by delta winglet vortex generators [21]; (c) a composite Trombe wall with or without PCM: the numerical study of a composite Trombe wall model both with and without PCM in relying on the Dymola/Modelica software [22], numerical studies of the comparison between two walls using sensible heat (with concrete as the storage wall) by means of TRNSYS software [23], experimental studies on the energy performance of a composite Trombe wall using concrete blocks as the storage element [24], an experimental study of a small-scale Trombe wall integrating the brick-shaped packages of PCM (hydrated salt) [25], and a theoretical study of a solar wall collector system on thermal performance [26]; and (d) a photovoltaic (PV) Trombe wall: applied in a one-room building model using TRNSYS software [27,28], a numerical study using FORTRAN to simulate the influence of photovoltaic glazing on the thermal and electrical performance of a photovoltaic-Trombe wall [29], a PV-Trombe wall assisted by a DC fan [30], a numerical study of the two-dimensional model of a PV glass panel [31,32], validation of the energy modeling of a building using computational fluid dynamics (CFD) and comparison of the system with a PV panel, single glass and double glass [33,34], experimental and numerical studies during winter correlated with a south facade design [35], and a numerical study of the periodic modeling of a semi-transparent photovoltaic thermal Trombe wall (SPVT-TW) in the winter season in New Delhi using MATLAB and R2013a software [36]. Moreover, physical phenomena occurring in this system were studied as well, i.e.: ventilated air layer effects, dimensional effects, storage wall effects, insulation wall effects, and glazing effects.

Generally speaking, the Trombe wall is constituted, on the outside, by glazing placed in front of the storage wall. These two components are separated by a small distance creating a ventilated or non-ventilated air layer and a greenhouse effect. The storage wall was initially made from concrete, stones, and bricks painted in dark colors on their outer surface [37]; its primary function is to absorb solar radiation (shortwave), with a portion of the absorbed energy being stored and then transferred to the interior space for heating during winter. The solar wall may, on occasion, be equipped with a vent open to the outside in order to generate air circulation (=chimney effect) from the inside to the outside in order to enhance the cooling of buildings at night during the summer[38].

In a classical Trombe wall, the low thermal resistance of the glazing can cause inverse thermocirculation in the ventilated air layer, thus decreasing room temperature during the night or non-sunny period and overheating it in the summer [24,39]. A redesign of the Trombe wall, known as the composite Trombe wall, took place [26]. Zalewski et al. presented the results from numerical and experimental studies conducted on four distinct types of passive solar walls [40]. Through comparing the results obtained, they were able to assist architects and project managers choose the most beneficial configuration for each type of building in response to specific climate conditions. Shen et al. modeled various solar walls using the finite difference method [26] in TRNSYS software to compare results between the classical Trombe wall and composite Trombe wall. They found that the model introduced was in a good agreement with measurement results; furthermore, they showed that the thermal energy performance of the composite Trombe wall was better than that of the classical wall during cold and/or

cloudy weather [23]. Nevertheless, the composite Trombe wall displays some disadvantages with respect to its low thermal energy storage and the problem of increasing the building's dead load when increasing (concrete or brick) storage wall volume [39].

To overcome these drawbacks while simultaneously improving efficiency of the composite Trombe wall, some studies replaced the classical (concrete or brick) storage wall with a high thermal capacity storage wall containing phase change materials (PCMs) [22,25]. PCMs store and release heat during their reversible cycles: solid-liquid (the most common in this kind of application), liquid-gas, or solid-solid; moreover, PCMs can absorb more energy than conventional materials for the same volume due to phase changes [41–43]. Thanks to their high latent heat storage, these materials have become the main topic of extensive research and have been widely developed and used in order to improve both thermal inertia and the time delay of released heat [43].

The first inclusion of phase change materials into Trombe walls took place around 1980 [44]. Bourdeau et al. [45] studied the behavior of a Trombe wall containing calcium chloride hexahydrate ($H_{12}CaCl_2O_6$) placed on a wooden frame behind a double-glazing. The results showed that for an equivalent effect, the latent heat storage wall can reduce 4 times the thickness of the concrete Trombe wall weighing a total of 6 times more than the PCM Trombe wall. Ghoneim et al. [18] performed the numerical simulation of a collector-storage wall incorporating various storage elements: sodium sulfate decahydrate ($Na_2 \cdot SO_4 \cdot 10\,H_2O$), medical paraffin, P116-wax, and classical concrete. Numerical results revealed that the Trombe wall containing PCM ($Na_2 \cdot SO_4 \cdot 10\,H_2O$) performed the thermal heat transfer with high efficiency compared to other storage elements (concrete, paraffin, P116-wax).

Khalifa et al. [46] modeled three thermal storage walls: concrete, hydrated salt ($CaCl_2 \cdot 6\,H_2O$), and paraffin-wax (N-eicosane); the imposed thermal boundary condition was based on Iraqi weather. Simulation results demonstrated that an 8-cm thick storage wall made of hydrated salt ($CaCl_2 \cdot 6\,H_2O$) could maintain the temperature in the interior zone close to the comfort level (22–25 °C), while a 20-cm thick concrete storage wall and a 5-cm thick paraffin storage wall were both affected by the ambient temperature, causing a decrease in the inside temperature (18–22 °C).

Fiorito [17] carried out an assessment of the thermal performance of a Trombe wall incorporating PCM. Five climatic environmental conditions were applied to evaluate sensitivity of the Trombe wall system. From the results obtained, PCM integration into a lightweight building component helped minimize the fluctuation of inside temperature for all climatic areas studied. Another research effort implementing DWVG (delta winglet vortex generators) on the outer surface of the storage wall containing PCM ($CaCl_2 \cdot 6\,H_2O$) is presented in [21]. The purpose of using this tool was to enhance heat transfer by convection; consequently, the results relative to airflow rate and room heating rate indicated that use of DWVG raised performance by 28.5% and 39.4%, respectively, compared to the case without DWVG.

Li et al. [47] tested a solar chimney system made of a Trombe wall integrating RT42 macro-encapsulated paraffin wax with three distinct imposed heat fluxes of 500 W/m², 600 W/m² and 700 W/m²; each experiment was run for 24 h. These experimental results showed that paraffin wax could efficiently store solar thermal energy during the day and release it several hours later; moreover, the duration of circulating air created from heat transfer exchanges could extend the period of released heat, especially at night, to around 14 h for all cases investigated.

Zhou et al. [48] studied the thermal performance of a newly ventilated Trombe wall integrating phase change materials (PCMs-VTW) as well as its optimization (melting temperature and PCM thickness) during the hot and cold season of a region set in China. The numerical model was used to simulate the energy performance of this newly ventilated Trombe wall. According to results, the energy storage and release efficiency (ESRE) achieved a 10% boost in summer and 13% in winter. This wall was further studied with respect to cooling performance with the PCMs embedded into the storage wallboard: the exterior PCM wallboard was to store cooling at night, whereas the interior PCM wallboard was to exchange radiant cooling. Results pointed to a reduction in energy consumption for cooling [49].

Alongside the development of the Trombe wall and in an attempt to reduce energy consumption in the building sector, a composite Trombe wall was developed both with and without PCM [22,25]. Zalewski et al. [25] tested a small-scale composite solar wall incorporating PCM (hydrated salts) conditioned in rectangular bricks. Test results underscored the high thermal energy storage of these hydrated salts ($H_2O + CaCl_2 + KCl$ + various additives), which can store much more heat than the same volume of concrete. The authors also proved that these bricks (thickness: 23 mm) allow recovering solar gains with a shorter time delay (approx. 2 h, 40 min), which had been the drawback in winter when a house wall required additional energy supply (i.e., heat gain) at the end of the day. Nevertheless, such a wall can be considered to be advantageous in winter when used for structures occupied during the day, e.g., offices, shopping centers, hospitals, universities, schools. Leang et al. [22] created a numerical model using the Dymola/Modelica software and its various libraries [50,51] in order to simulate two cases of a solar wall component. The first case sought to compare experimental and numerical results for a composite Trombe wall equipped with a concrete storage wall as a means of validating the model. The second case was intended to use the validated model to conduct other simulations of the composite Trombe wall, in which concrete was replaced by a wall integrating micro-encapsulated PCM.

Recent studies focused on implementing PCMs as thermal energy storage into the hybrid system with active cooling and hybrid ventilation. Zhou et al. [52] studied the numerical modeling of a system of hybrid PCMs working on the one hand as a ventilated Trombe wall integrating phase change materials (PCMs-VTW) and on the other as a photovoltaic/thermal system integrating a phase change material (PV/T-PCM). Based on the results obtained, the system is able to provide a stable indoor thermal environment. This new hybrid system incorporating PCMs was then investigated with the machine learning-based, data-driven model in order to predict on-site renewable electricity generation [53–55], which involved system parameter optimization [56].

The scientific gaps herein pertain to: the lack of research on integrating phase change materials (PCMs) into the composite Trombe wall system to allow storing and releasing thermal energy with latent heat; and the absence of numerical studies simulating the thermal performance of this solar wall in the Dymola/Modelica library. Furthermore, the aforementioned study regarding the numerical model with Dymola/Modelica does present the thermal performance of a composite solar wall integrating the concrete storage wall with storage and release in the form of sensible heat. This study will present a small-scale composite Trombe wall integrating phase change materials; its main objectives are as follows:

1. Present the specific features and experimental set-up of a composite Trombe wall containing PCM;
2. Explain how the numerical method, with the help of the Dymola/Modelica software, performs in determining the thermal behavior of the composite solar walls;
3. Validate this numerical model based on a comparison between simulation and measurement;
4. Compare the efficiency of sensible vs. latent storage of composite solar walls.

2. Composite Solar Wall and Experimental Set-Up

Figure 1 shows the diagram of the composite Trombe wall studied herein and designed to heat living areas. The operating mode of this solar wall is passive and conforms to a low-cost configuration. From the outside, in the presence of solar radiation, glazing creates a greenhouse effect in a non-ventilated air gap that increases the PCM wall temperature. The main characteristics of the outer storage wall surface are the solar absorption coefficient α, which depends on the wall surface color, and the emissivity ε.

The energy absorbed by the opaque wall is stored and then transferred with a time delay to the ventilated air gap between the storage wall and the insulating wall. The ventilated air layer plays a significant role in the ability to recover thermal energy transmitted to the room. An insulating panel serves to avoid both energy losses during periods when solar gains are insufficient and overheating in summer. However, during summertime, it is advisable to add a sunscreen in front of the glazing. The insulating panel is perforated to allow natural air thermocirculation through the lower and upper

vents. In some cases, a system designed to avoid reverse thermocirculation in the ventilated air layer can be installed. A flexible plastic film placed over the lower vent was studied and proven to be effective in preventing a reverse thermosiphon with minimal air flow disruption [24,57]. This experimental set-up does not feature a system to block reverse thermocirculation because the primary aim here is to study exchanges in the ventilated layer.
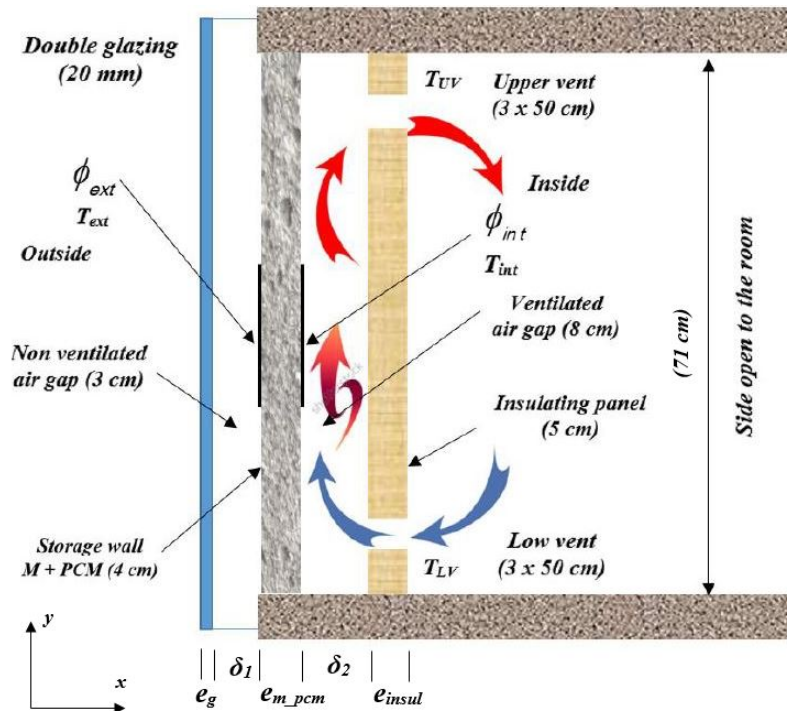

Figure 1. Vertical cross-section of the experimental set-up.

The experimental set-up, assembled on a reduced scale 83 cm high, 73 cm wide and 1 m deep, was placed on the south side of the laboratory. The dimensions of the storage wall were: $71 \times 59 \times 4$ cm^3.

Figure 2 shows the solar wall set-up. It is equipped with thermocouples (T-type-diameter: 0.1 mm) to measure air and surface temperatures, plus two heat fluxmeters (tangential gradient type) to measure heat flux evolution on both sides of the storage wall. The calibration procedure, described in [58,59], provides these sensors with an accuracy of $\pm 3\%$. The pyranometer is located in the vertical plane of the facade receiving incident solar flux. Since our laboratory window is set above the first floor, which has a white roof, the solar wall is able to benefit from the influence of solar reflection and thus receives higher solar radiation. The two heat fluxmeters with an integrated thermocouple (ϕ_{ext}, T_{ext}, ϕ_{int} and T_{int}) are placed on both sides of the storage wall in the central position (Figure 1). The fluxmeter (ϕ_{ext}) measures the flux of heat entering or leaving the outer storage wall surface (solar radiation and exchanges between the storage wall and glazing). On the ventilated air layer side, the fluxmeter (ϕ_{int}) simultaneously measures the convective exchanges between storage wall and air as well as the radiative exchanges between this same wall and the insulated wall located opposite. Two thermocouples measure air temperature at both the lower vent (T_{lv}) and the air layer outlet at the upper vent (T_{uv}).
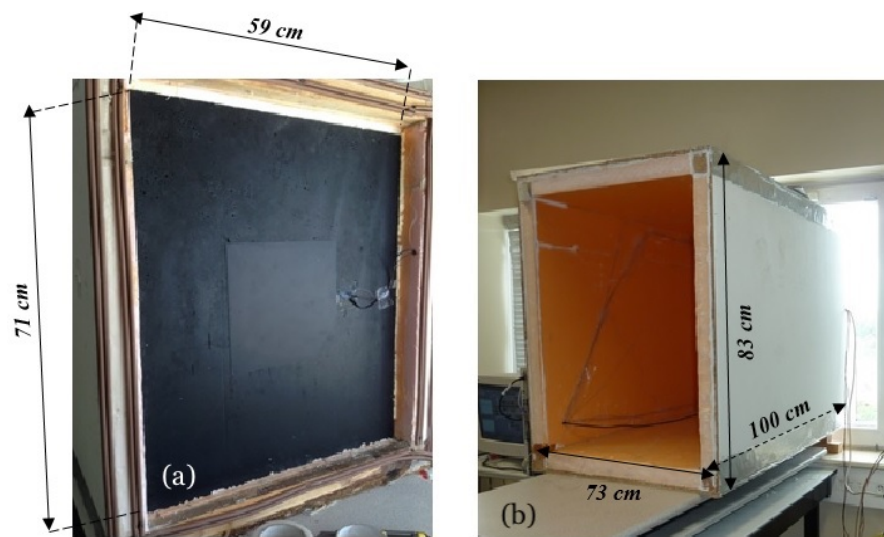
Figure 2. External view of the storage wall (**a**), and rear view of the experimental solar wall (**b**).

3. Meteorological Data

The meteorological data used herein was recorded on a prototype built in northern France (50°30'57.4" N latitude, 2°39'24.2" E longitude) from 19th April to 26th 2014. This period lies in the best season for solar home heating systems because solar gains are significant while outside temperatures remain quite low. The incident global solar radiation on the vertical facade of the building was measured by a pyranometer (CMP10-kipp and zonen) (Figure 3). The outside temperature was measured by a thermocouple inserted into a cylinder painted white and naturally ventilated, and wind speed was measured by an anemometer/wind vane installed near the facade containing the composite Trombe wall (Figure 4). All measurements were recorded with a time step of 5 min.

Figure 3. Pyranometer used to measure the global vertical solar radiation.
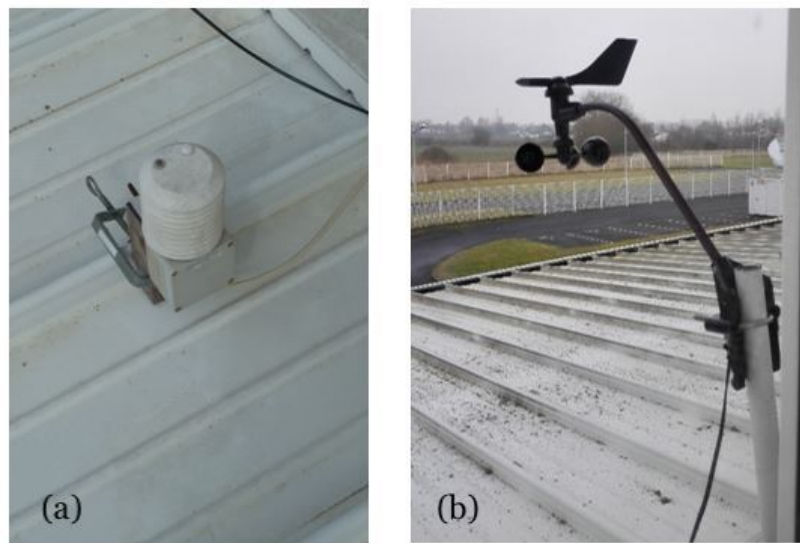
Figure 4. Sensors used to measure outside temperature (**a**) and anemometer/wind vane used to measure wind speed and direction (**b**).

The results of global solar flux measurements on the vertical facade, outdoor temperature and wind speed are shown in Figures 5 and 6. Please note that the solar flux values may appear to be high (1000 W/m^2); this is due to the presence of a horizontal light-colored roof under the windows of the floor where the experiments were carried out (Figure 4).
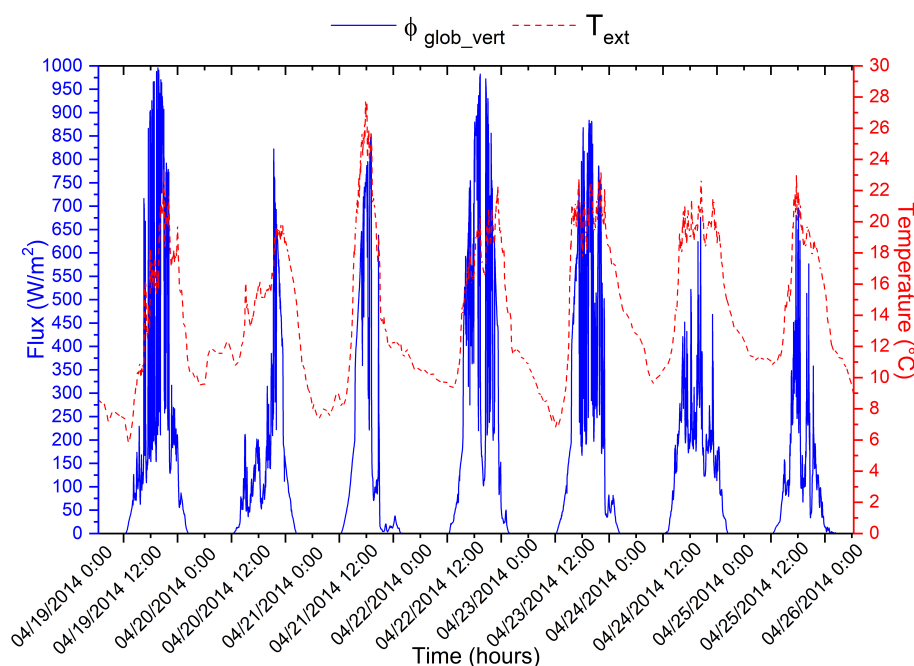

Figure 5. Meteorological data: ϕ_{glob_vert} denotes global solar radiation on the vertical facade of the wall, and T_{ext} denotes outside air temperature.
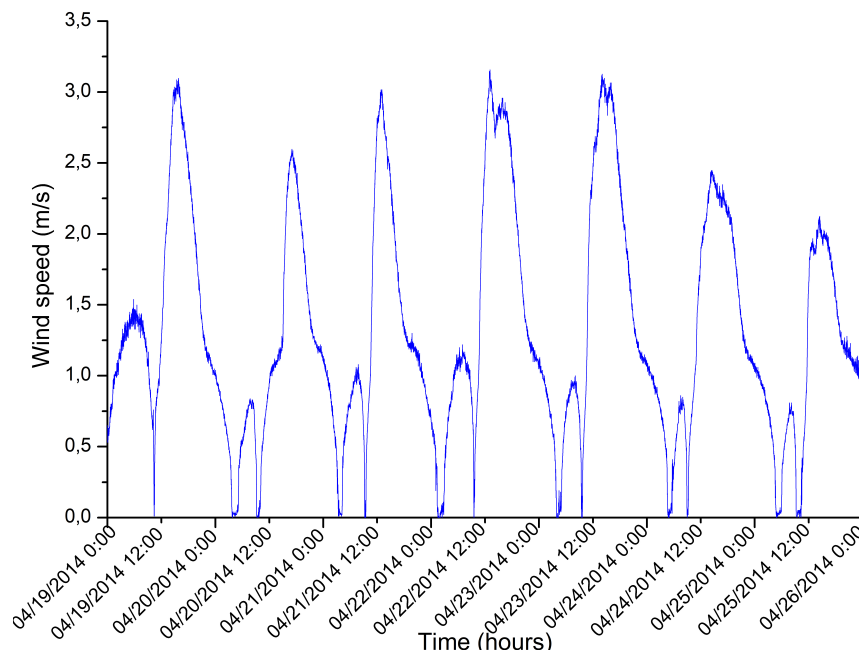
Figure 6. Wind speed measured by the anemometer/wind vane.

4. Mathematical Model

Figure 7 shows the diagram of the model components used for the composite Trombe wall and the boundary conditions (both exterior and interior) imposed in the Dymola/Modelica software. In this model, some of the elements introduced stemmed from the "Buildings", "IDEAS" and "Modelica" libraries [50,51], namely: PrescribedTemperature, PrescribedHeatFlow, Convection, HeatCapacitor, ThermalConductor, CombiTimeTable, and Integrator. In contrast, other elements were created, e.g.: ϕ_{glass1}, ϕ_{glass2}, ϕ_{wall}, glass1, glass2, storage wall with/without PCM, insulating panel, ventilated air layer. The most interesting point here is implementation of the model focused on the latent storage wall and based on the enthalpy method. The typical procedure for running Dymola/Modelica is to graphically build a model by selecting, drawing, connecting and configuring the individual components extracted from a library. The meteorological data are stored in tables, while the codes (formulas and equations) representing the physical behavior of the various model parts (convection, radiation, conduction) are embedded in the components:

- ϕ_{glass}: evaluate the solar heat flux absorbed by glazing and the direct flux transmitted to the outer storage wall surface M+PCM Equation (14);
- ϕ_{wall}: evaluate the total energy absorbed by the wall in considering the heat flux transmitted from the glazing and multi-reflections in the non-ventilated air gap Equation (15);
- Rad_ext: evaluate the longwave radiation exchange with the sky (radiative diffusion) and the radiation reflected by the roof of the lower floor located under the window on the facade Equations (3) and (4);
- Conv_ext: evaluate the total heat transfers by convection between the composite Trombe wall and the outside. This step depends on the outdoor air temperature as well as the wind velocity and direction Equation (6);
- Conv_int: evaluate the total heat transfers by convection between the inner wall facade and the indoor environment Equations (36) and (37);
- Rad_int: evaluate the inside longwave radiative heat transfer between the inner wall facade and the indoor environment Equation (35);
- exchange_rad: evaluate the inside longwave radiative heat transfer between the inner and outer surfaces of glass1 and glass2, glass2 and storage wall, and storage wall and insulating panel Equations (11) and (24);

- exchange_conv: evaluate the inside heat transfer by convection between the inner and outer surfaces of glass1 and glass2, and glass2 and storage wall Equations (12) and (13);
- ventilated air layer: evaluate the heat transfer by convection between the surfaces of the storage wall and insulating panel to the circulating fluid, along with the mass flow rate of the fluid, and the power released from the solar wall Equations (25), (26), (30) and (32).
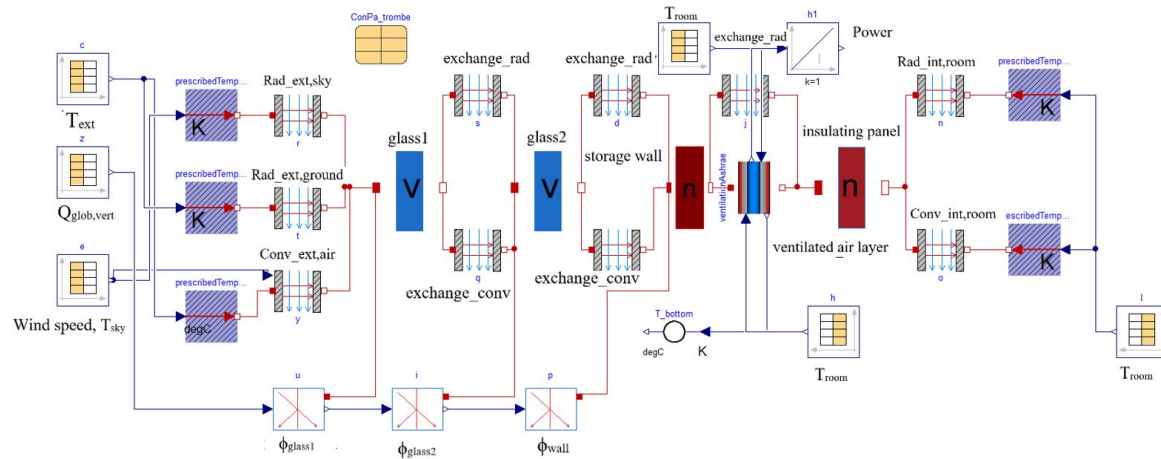

Figure 7. Diagram of a composite Trombe wall model using the Dymola/Modelica software.

4.1. Thermal Balance on the External Glazing Surface

On the outer glazing surface, the heat transfers by both radiation and convection are considered (Equation (1)). These superficial heat transfers are linearized using the gray surfaces hypothesis in longwave radiation. In this case, the following expression for the thermal balance at the outer solar wall is thus obtained:

$$\phi_g|_{x=0} = \alpha_g Q_{glob,vert} + Q_r + Q_{conv} \tag{1}$$

where $Q_{glob,vert}$ is the vertical global solar flux on the outer surface of the double glazing; this flux is the sum of the various components of the incident solar radiation that reaches the surface of the double glazing (direct, diffuse and reflected radiation).

Q_r is the balance of longwave radiation exchanges between the surface of the double glazing and its external environment (ground environment and celestial vault); this total flux is given by the following equation:

$$Q_r = h_{r,sky}(T_{sky} - T_{g,ext}) + h_{r,gro}(T_{gro} - T_{g,ext}) \tag{2}$$

where:

$$h_{r,sky} = \frac{\sigma \left(T_{sky}^2 + T_{g,ext}^2\right)\left(T_{sky} + T_{g,ext}\right)}{1/\varepsilon_{g,ext} + 1} \tag{3}$$

$$h_{r,gro} = \frac{\sigma \left(T_{gro}^2 + T_{g,ext}^2\right)\left(T_{gro} + T_{g,ext}\right)}{1/\varepsilon_{g,ext} + 1} \tag{4}$$

$h_{r,sky}$ and $h_{r,gro}$ are the radiative heat transfer coefficients on the outer surface of the double glazing. $h_{r,sky}$ and $h_{r,gro}$ are calculated based on the fluctuation between the sky temperature, the outside air temperature (T_{sky}, T_{gro}) and the glass temperature ($T_{g,ext}$).

Q_{conv} is the convective heat transfer at the outer surface of the double glazing with the outside air; it is calculated by the following equation:

$$Q_{conv} = h_{c,g}\left(T_{env} - T_{g,ext}\right) \tag{5}$$

The convective heat transfer coefficient at the outer surface of the double glazing is then calculated by the correlation [60]:

$$h_{c,g} = \frac{2 \times 0.86 \lambda_f \left(Re^{1/2} \right) \left(Pr^{1/3} \right)}{H + W} \tag{6}$$

where:

$$Re = \frac{V \left(H + W \right)}{2 v_{air}} \quad and \quad Pr = \frac{\mu_{air} c_{air}}{\lambda_{air}} \tag{7}$$

Hence, the thermal balance on the outer surface of the solar wall equipped with double glazing is:

$$\phi_g|_{x=0} = \alpha_g Q_{glob,vert} + h_{r,sky}(T_{sky} - T_{g,ext}) + h_{r,gro}(T_{gro} - T_{g,ext}) + h_{c,g} \left(T_{env} - T_{g,ext} \right) \tag{8}$$

4.2. Thermal Balance on the Inner Surface of the Glazing (Non-Ventilated Air Gap)

In the non-ventilated air layer between the inner surface of the glazing ($x = e_g$) and the outer storage wall surface ($x = e_g + \delta_1$), the average temperature of fluid T_{f1} is set equal to the average glazing and storage wall surface temperatures: $T_{f1} = (T_g + T_w)/2$. The thermal balance of the two walls (glazing and storage wall) is calculated by the following equations:

$$\phi_g|_{x=e_g} = h_{r1} \left(T_{w,ext} - T_{g,int} \right) + h_{c1} \left(T_{f1} - T_{g,int} \right) + \xi_g Q_{glob,vert} \tag{9}$$

$$\phi_w|_{x=e_g+\delta_1} = h_{r1} \left(T_{g,int} - T_{w,ext} \right) + h_{c1} \left(T_{f1} - T_{w,ext} \right) + \xi_w Q_{glob,vert} \tag{10}$$

h_{r1} is the radiative heat transfer coefficient between the two surfaces (glazing and storage wall):

$$h_{r1} = \frac{\sigma \left(T_{w,ext}^2 + T_{g,int}^2 \right) \left(T_{w,ext} + T_{g,int} \right)}{1/\varepsilon_{g,int} + 1/\varepsilon_{w,ext} - 1} \tag{11}$$

The convective heat transfer coefficient h_{c1} in the non-ventilated air gap between the two walls is now calculated from the Hallands and Buchberg correlations [61,62]:

$$Nu = \frac{h_{c1}H}{\lambda_{f1}} = max \left\{ 1, 0.288 \left(\frac{Ra.W}{H} \right)^{1/4}, 0.039 \left(\frac{Ra.W}{H} \right)^{1/3} \right\} \tag{12}$$

$$Ra = Gr_{f1}.Pr_{f1} = \left(\frac{\beta_{f1} g \rho_{f1}^2 \delta_1^3 \left| T_g - T_w \right|}{\mu_{f1}^2} \right) \left(\frac{\mu_{f1} c_{f1}}{\lambda_{f1}} \right) \tag{13}$$

To increase the effectiveness of the wall, several parameters characteristic of the exterior cover become important, namely: the global transmission coefficient of double glazing τ and the emissivity factor ε significantly influence both the solar radiation absorption by the opaque wall and the limitation of thermal heat loss. Due to multi-reflection between the two walls of the non-ventilated air layer, ξ_g and ξ_w indicate the global coefficients of total fluxes of incident shortwave solar radiation absorbed by glazing and wall:

$$\xi_g = \frac{\tau_{g1} \alpha_{g2}}{1 - \rho_{g2} \rho_{g1}} + \frac{\tau_{g1} \tau_{g2} \rho_w \alpha_{g2}}{1 - \rho_w \rho_{g2}} \left(1 + \frac{\rho_{g2} \rho_{g1}}{1 - \rho_{g2} \rho_{g1}} \right) \tag{14}$$

$$\xi_w = \frac{\tau_{g1} \tau_{g2} \alpha_w}{1 - \rho_w \rho_{g2}} + \left(\tau_{g1} \tau_{g2} \alpha_w + \frac{\tau_{g1} \tau_{g2}^3 \rho_w \rho_{g1} \alpha_w}{1 - \tau_{g2}^2 \rho_w \rho_{g1}} \right) \tag{15}$$

4.3. Thermal Transfer by Conduction on the Storage Wall

The method used to model the thermal behavior of the latent storage wall was presented in several articles [63–65]; it consists of characterizing by the inverse method the parameters required

to model the heat transfer of a mortar integrating a micro-encapsulated PCM during the phase change (solid <–> liquid). To establish the state equations of the composite material (mortar + PCM), the thermodynamic behavior of the PCM could be assimilated to that of a binary solution. Since the PCM is micro-encapsulated, the assumptions here stipulate no natural convection in the microcapsules given that their dimensions vary between 5 and 40 μm and are uniformly distributed in the cement mortar matrix. The model implemented in the Dymola/Modelica software was based on the enthalpy derivative equation (Equation (16)) [66].

$$\frac{\partial \rho h}{\partial t} = \lambda \frac{\partial T^2}{\partial^2 x} \tag{16}$$

This model depicts the unidirectional conduction of a homogeneous mono-layer material under transient conditions. The discretization is performed by assigning for each mesh two resistances and a capacity that varies with temperature (see Figure 8):

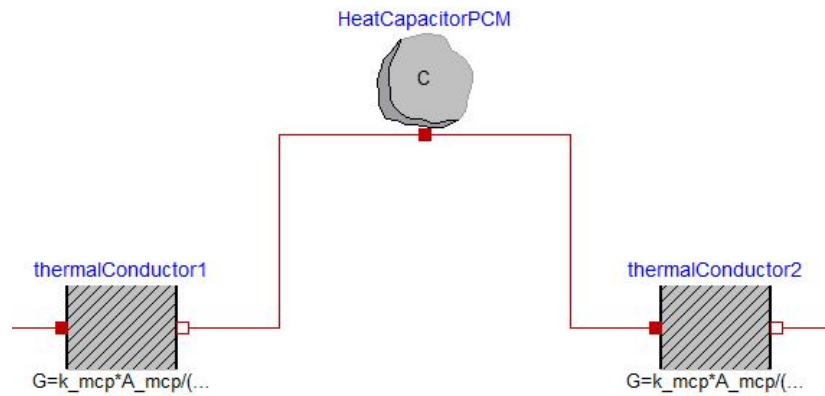$$C\frac{dT}{dt} = \phi_i - \phi_{i+1} \tag{17}$$

Figure 8. Model of a phase change material mesh.

The wall is then discretized into a 1D mesh, in which the heat balance can be calculated using the following equations (Equation (18)):

$$\phi_i = \left(\frac{\lambda.A}{e_{mesh}/2}\right)dT_i \quad and \quad \phi_{i+1} = \left(\frac{\lambda.A}{e_{mesh}/2}\right)dT_{i+1} \tag{18}$$

Each mesh possesses the same thermal properties (λ, c, ρ) and thickness (e_{mesh}). After a parametric study, a discretization of 30 meshes was selected. The thermophysical and dimensional properties introduced are those of the apparent composite material, which means that the composite material resulting from the mixture of cement mortar and PCM is considered to be a homogeneous isotropic material:

$$\phi_i = \left(\frac{\lambda_{m\_pcm}.A_{m\_pcm}}{e_{mesh.m\_pcm}/2}\right)dT_i \quad and \quad \phi_{i+1} = \left(\frac{\lambda_{m\_pcm}.A_{m\_pcm}}{e_{mesh.m\_pcm}/2}\right)dT_{i+1} \tag{19}$$

It is necessary therefore to determine the enthalpy curve h(T). The enthalpy curve of a binary solution without a eutectic is of the form shown in Figure 9a. The formulation of this curve involves the end of the melting temperature (T_M), the melting temperature associated with the pure substance (T_A) of the PCM, the specific heats of the composite material when the PCM is in the solid state (c_{solid}) and in the liquid state (c_{liquid}), as well as the latent heat of phase change (L_A) contained in the composite material.

The heat stored in the storage wall integrating PCM (mortar PCM) represents the latent heat in considering both its melting and solidification. For this storage wall, c_{m_pcm} represents the derivative of

enthalpy with respect to temperature T [63,66] and is presented in Figure 9b. The following equations are used to determine the value of c_{m_pcm} once the material temperature is known.
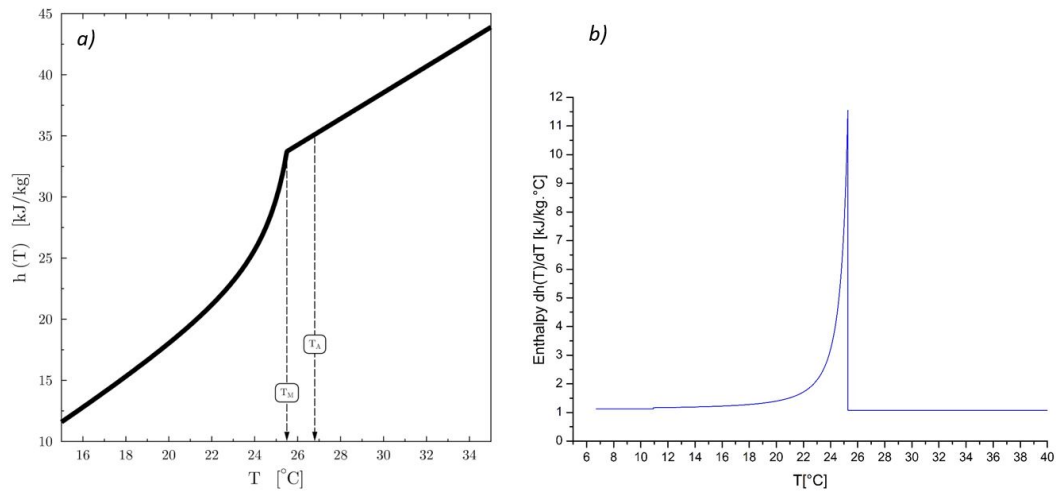

Figure 9. (**a**) Enthalpy curve vs. temperature, (**b**) Derivative of the enthalpy vs. temperature T.

$$C = c_{m\_pcm} . A_{m\_pcm} . e_{m\_pcm} . \rho_{m\_pcm} \tag{20}$$

$$c_{m\_pcm} = \frac{dh_{m\_pcm}}{dT} = \begin{cases} \left(\dfrac{T_A - T_M}{T_A - T}\right) c_{liquid} + \left(1 - \dfrac{T_A - T_M}{T_A - T}\right) c_{solid} + L_A \dfrac{T_A - T_M}{(T_A - T)^2} & \text{if } T < T_M \\[4mm] c_{liquid} & \text{if } T \geq T_M \end{cases} \tag{21}$$

4.4. Thermal Balance in the Ventilated-Air Layer

The thermal balance in the ventilated air layer is considered to be a heat transfer by convection between the wall surfaces and the circulating air, as well as a heat exchange by radiation between the inner and outer surfaces of the storage wall and insulating panel:

$$\phi_w|_{x=e_g+\delta_1+e_{m\_pcm}} = h_{r2} \left(T_{ins,ext} - T_{w,int}\right) + h_{c2} \left(T_{f2} - T_{w,int}\right) \tag{22}$$

$$\phi_{ins}|_{x=e_g+\delta_1+e_{m\_pcm}+\delta_2} = h_{r2} \left(T_{w,int} - T_{ins,ext}\right) + h_{c2} \left(T_{f2} - T_{ins,ext}\right) \tag{23}$$

where:

$$h_{r2} = \frac{\sigma \left(T_{w,int}^2 + T_{ins,ext}^2\right)\left(T_{w,int} + T_{ins,ext}\right)}{1/\varepsilon_{w,int} + 1/\varepsilon_{ins,ext} - 1} \tag{24}$$

The convective heat transfer coefficient of the fluid movement is calculated using Churchill correlations [67]:

$$Nu = \frac{h_{c2}H}{\lambda_{f2}} = \begin{cases} 0.68 + \dfrac{0.67 Ra^{1/4}}{\left(1 + \left(\dfrac{0.492}{Pr}\right)^{9/16}\right)^{4/9}} & Ra < 10^9 \\[8mm] \left(0.825 + \dfrac{0.387 Ra^{1/6}}{\left(1 + \left(\dfrac{0.492 Ra^{1/6}}{Pr}\right)^{9/16}\right)^{8/27}}\right)^2 & Ra > 10^9 \end{cases} \tag{25}$$

where:

$$Ra = Gr_{f2}.Pr_{f2} = \left(\frac{\beta_{f2} g \rho_{f2}^2 \delta_2^3 \left| T_p - T_{f2} \right|}{\mu_{f2}^2} \right) \left(\frac{\mu_{f2} c_{f2}}{\lambda_{f2}} \right) \tag{26}$$

Panel temperature: $T_p = T_w$ for storage wall, and $T_p = T_{ins}$ for insulating wall. In this study, considering the dimension and weather conditions, the Rayleigh number remains below the limits of (10^9). Therefore, the correlation considered for all calculations is the first one during the measurement period.

Temperature T_{f2} of the air-fluid circulating in the ventilated air layer depends on the heat fluctuations released from the two wall surfaces (storage and insulating walls) and the inlet air temperature at the lower (or upper) vent of the ventilated air layer. The numerical method used to calculate this average air-fluid temperature is given in [57]:

$$T_{f2} = \left(\frac{1}{a_0 H} - \frac{e^{-a_0 H}}{(1 - e^{-a_0 H})} \right) T_{inlet} + \left(-\frac{1}{a_0 H} + \frac{1}{(1 - e^{-a_0 H})} \right) T_{outlet} \tag{27}$$

$$T_{outlet} = T_{inlet}.e^{-a_0 H} + \frac{b_0}{a_0} \left(1 - e^{-a_0 H} \right) \tag{28}$$

where:

$$a_0 = \frac{h_{c2,w} W + h_{c2,ins} W}{\dot{m} c_{f2}} \; ; \; b_0 = \frac{h_{c2,w} W T_w + h_{c2,ins} W T_{ins}}{\dot{m} c_{f2}} \tag{29}$$

The airflow rate $\dot{m}$ results from the fluctuations in temperatures T_{inlet} and T_{outlet}, and the total head loss coefficient of fluid during its natural thermocirculation in the ventilated layer. This entire analysis was detailed in [23,57]. The airflow rate $\dot{m}$ can be calculated using the following equations:

$$\dot{m} = \rho_{f2} A \left(\frac{2gH}{\zeta_{total}} \left(\frac{T_{outlet} - T_{inlet}}{T_{outlet} + T_{inlet}} \right) \right)^{1/2} \tag{30}$$

$$\zeta_{total} = \zeta_{entry}.\rho_{f,bottom} \left(\frac{\rho_{f2} A_{air\_gap}}{\rho_{f,bottom} A_{lv}} \right)^2 + \zeta_{lv,bottom}.\rho_{f,bottom} \left(\frac{\rho_{f2} A_{air\_gap}}{\rho_{f,bottom} A_{lv}} \right)^2 \tag{31}$$

$$+\zeta_{elbow\,bottom}.\rho_{f,bottom} \left(\frac{\rho_{f2} A_{air\_gap}}{\rho_{f,bottom} A_{lv}} \right)^2 + \zeta_{linear}.\rho_{f2} + \zeta_{elbow\,top}.\rho_{f2}$$

$$+\zeta_{uv}.\rho_{f,top} \left(\frac{\rho_{f2} A_{air\_gap}}{\rho_{f,bottom} A_{uv}} \right)^2 + \zeta_{out}.\rho_{f,top} \left(\frac{\rho_{f2} A_{air\_gap}}{\rho_{f,top} A_{uv}} \right)^2$$

It then becomes possible to validate the accuracy of correlations used in the calculation and summation of heat fluxes measured from the fluxmeter:

$$P_{cal} = \dot{m} c_{f2} \left| T_{outlet} - T_{inlet} \right| \tag{32}$$

$$P_{flux} = \sum \phi A_{exch} \tag{33}$$

4.5. Thermal Balance towards the Interior Atmosphere

The thermal transfer by convection and radiation between the insulating wall and indoor air is estimated as follows:

$$\varphi_{ins} \big|_{x=e_g+\delta_1+e_{m\_pcm}+\delta_2+e_{ins}} = h_{r,amb} \left(T_{amb} - T_{ins,int} \right) + h_{c,ins} \left(T_{amb} - T_{ins,int} \right) \tag{34}$$

where:

$$h_{r,amb} = \sigma \varepsilon_{ins,int} \left(T_{amb}^2 + T_{ins,int}^2 \right) \left(T_{amb} + T_{ins,int} \right) \tag{35}$$

The coefficient of heat exchange by convection between the insulating wall and ambient air is calculated from MacAdams' correlation [68]:

$$Nu = \frac{h_{c,ins}H}{\lambda_{f,amb}} = \begin{cases} 0.56Ra^{1/4} & 10^4 < Ra < 10^8 \\ 0.13Ra^{1/3} & 10^8 < Ra < 10^{12} \end{cases} \tag{36}$$

$$Ra = Gr_{ins}.Pr_{ins} = \left(\frac{\beta_{f,amb}gH^3\left|T_{ins} - T_{f,amb}\right|}{v_{f,amb}^2} \right) \left(\frac{\mu_{f,amb}c_{f,amb}}{\lambda_{f,amb}} \right) \tag{37}$$

4.6. Material Properties

The storage wall used in the composite Trombe wall was produced with cement mortar (CM) made from a mix of sand (round silica sand 0-4 mm), cement (EMC I 52.5 N, according to EN 196-1), water and micro-encapsulated PCM (Micronal® PCM DS 5001 X) at a proportion of mixed cement mortar in 17 % of the total mass of dry materials (sand, cement, PCM). The mix proportions are listed in Table 1.

Table 1. Mix proportion of cement mortar integrating PCM Micronal®.

Cement-Sand Mass Ratio	Water to Cement Ratio	PCM/(Cement + Sand) Mass Ratio
1/2.6	1/1.1	1/4.1

The mixture was poured into a mold and dried for more than two months in our laboratory. One storage element was ultimately built with the following dimensions: 4 cm thickness (mortar incorporating PCM), 59 cm width, and 71 cm height (65 cm from lower to upper vent). The thermal properties were characterized by applying the enthalpy method described and improved in previous articles [63–66]. The thermophysical properties of the materials constituting the composite Trombe wall are presented in Table 2.

Table 2. Thermophysical properties of the materials employed.

Material	Symbol	Explanation	Unit	Value
Glazing	ρ_g	density	kg/m^3	2500
	c_g	specific heat capacity	J/(kg.K)	830
	λ_g	thermal conductivity	W/(m.K)	1.47
	α_g	absorptivity	-	0.84
	τ_g	transmissivity	-	0.76
	ε_g	emissivity	-	0.84
Mortar + PCM	ρ_{m_pcm}	density	kg/m^3	1329
	c_{solid}	specific heat at solid state	J/(kg.K)	1178
	c_{liquid}	specific heat at liquid state	J/(kg.K)	1150
	L_A	latent heat	J/kg	17100
	T_A	pure substance temperature	°C	27.37
	T_M	melting temperature	°C	25.83
	λ_{m_pcm}	thermal conductivity	W/(m.K)	0.62
	α_{m_pcm}	absorptivity	-	0.9
	ε_{m_pcm}	emissivity	-	0.9
Insulating wall	ρ_{ins}	density	kg/m^3	30
	c_{ins}	specific heat capacity	J/(kg.K)	880
	λ_{ins}	thermal conductivity	W/(m.K)	0.041
	α_{ins}	absorptivity	-	0.9
	ε_{ins}	emissivity	-	0.9

5. Model Validation, Results and Discussion

The calculations were performed with a time step equal to that of the data acquisition, i.e., 5 min, over a one-week duration. Figures 10 and 11 show respectively the comparison of numerical and experimental heat fluxes and temperatures on both sides of the storage wall (cement mortar + PCM). The composite Trombe wall was equipped with fluxmeters and thermocouples in order to measure the fluctuation in heat flux and temperature. When the solar flux radiation reaches its highest intensity, varying from 950 to 1000 W/m^2 (Figure 5), the storage wall can absorb a large quantity of incoming solar flux (400–450 W/m^2 of heat flux at the external surface of the storage wall), corresponding to about 50% of the incident solar radiation during sunshine hours. This percentage confirms the transmission rate measurements conducted in our laboratory with two pyranometers placed on both sides of the double glazing. The heat flux becomes negative (-50 W/m^2) at the outer surface of the storage wall by the end of the day due to heat losses into the external environment. It should be noted here that the semi-transparent cover is a conventional double glazing; a glass with reinforced insulation would certainly have made it possible to limit these heat losses. The time lag between the incident solar radiation and the heat flux release in the ventilated air layer (ϕ_{int}), for this 4-cm thick experimental storage wall, is estimated by calculating the cross-correlation function [24] at 184 min (i.e., approximately 3 h). During sunny periods, the storage wall temperature can reach 65 $°C$ on the outer surface and 45 $°C$ on the inner surface.

The difference between the heat fluxes at the outer surface of the storage wall ϕ_{ext}, as calculated by the numerical method and measured by the fluxmeters (sum of the absolute values of the heat fluxes) equals 2.2%. This value is on the order of 8.6% of the difference evaluated between the calculations and measurements of heat fluxes on the inner surface of the storage wall, ϕ_{int}. The average difference between the calculated and measured temperatures on the outer and inner surfaces of the storage wall (T_{ext} and T_{int}) is on the order of 1 $°C$. The difference of 8.6% between the calculated and measured flows on the inner side of the storage wall is due to the less accurate estimation of temperature on this surface, which is especially true at maximum temperatures. This difference is most probably due to the unidirectional (1D) calculation of heat transfers in the wall; consequently, heat losses towards the edges of the storage wall are not being taken into account. Moreover, the difference between numerical calculation and thermocouple measurement of the air temperature at the upper vent level of the ventilated air layer T_{uv} is on average 0.4 $°C$. In Figure 11, the released latent heat can be observed every day around 8:00 pm by the inflection of temperature curves at 26 $°C$, corresponding to the solidification point.

Figure 12 illustrates air temperature variations at the inlet (T_{lv}) and outlet (T_{uv}) of the ventilated air layer, as well as the ambient temperature of the room (T_{room}). When the average temperature of air inside the ventilated air layer is higher or warmer than the room air temperature, a natural thermocirculation is thus activated, with air entering through the lower vent (T_{lv}) and being released from the upper vent (T_{uv}). This phenomenon is due to the thermal contributions of the storage wall in the ventilated air layer (convection and radiation), which in turn cause the air to be heated and then set into motion (i.e., a thermosiphon or "chimney effect"). During its movement towards the upper vent, the air is warmed up in contact with the storage wall before being introduced into the room; a very small portion of the energy supplied by the solar wall is transmitted to the room by means of conductive heat transfer through the insulating wall. On the other hand, during non-sunny periods or at the end of the night, when heat flux at the external surface of the storage wall is negative, the storage wall discharges its thermal energy towards the outside and becomes colder than the air in the room. As a consequence, the air circulating in the ventilated air layer during the inverse thermocirculation is affected by this convective heat transfer, in turn decreasing the air temperature. When the storage wall is cooler than the indoor environment, air enters through the upper vent, cools in contact with the walls, becomes heavier and returns to the room through the lower vent of the ventilated air layer. In this case therefore, a reverse thermocirculation effect is at work.
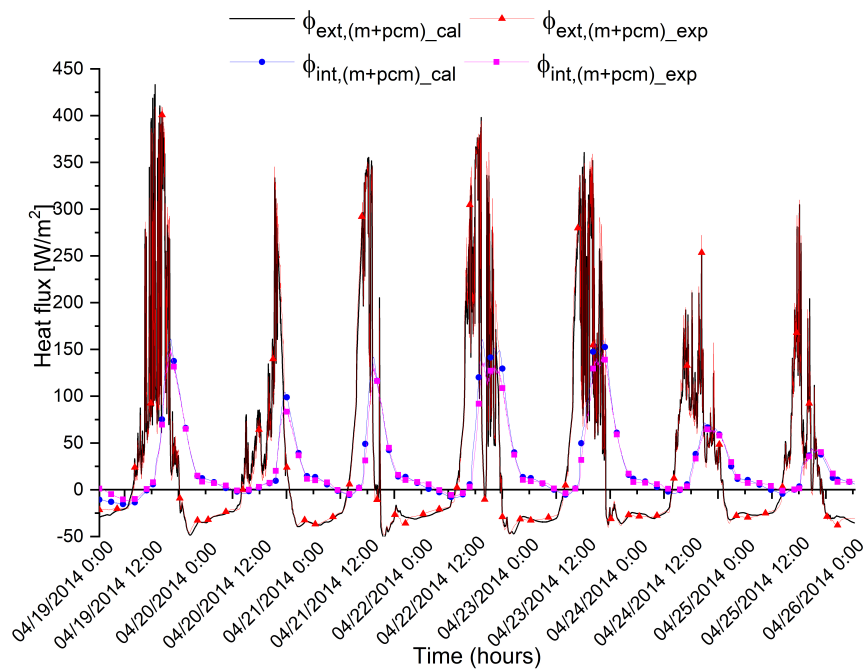
Figure 10. Comparison of heat fluxes on both sides of the storage wall (model results and experimentation). $\phi_{ext,(m+pcm)\_cal}$ and $\phi_{ext,(m+pcm)\_exp}$ denote respectively the evolution in numerical and experimental heat fluxes on the exterior surface of the storage wall containing PCM; $\phi_{int,(m+pcm)\_cal}$ and $\phi_{int,(m+pcm)\_exp}$ denote respectively the evolution in numerical and experimental heat fluxes on the interior surface of the storage wall containing PCM.
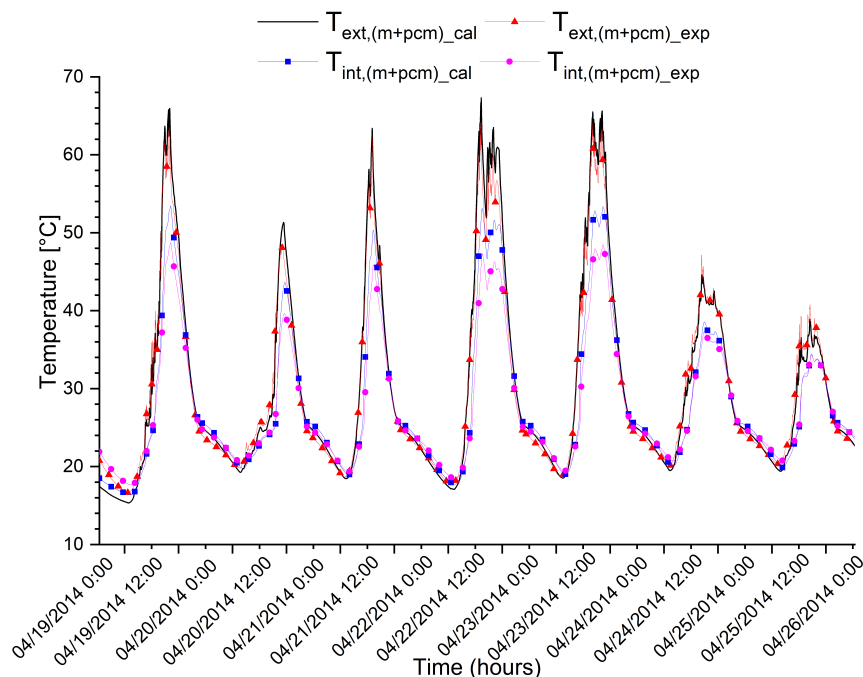

Figure 11. Comparison of temperatures on both sides of the storage wall (model results and experimentation). $T_{ext,(m+pcm)\_cal}$ and $T_{ext,(m+pcm)\_exp}$ denote respectively the evolution in numerical and experimental temperatures on the exterior surface of the storage wall containing PCM; $T_{int,(m+pcm)\_cal}$ and $T_{int,(m+pcm)\_exp}$ denote respectively the evolution in numerical and experimental temperatures on the interior surface of the storage wall containing PCM.

To identify the airflow direction, it is sufficient to observe what temperature between T_{lv} and T_{uv} is closest to the room air temperature (T_{room}). A negative heat flux sign on the inner surface of

the storage wall (ϕ_{int}) makes it possible to identify this phenomenon. For our model, the following conditions must be input in order to define the air flow direction: if $T_{air\ layer} > T_{room}$, air enters at the lower vent of the composite solar wall and heats the room; if $T_{air\ layer} < T_{room}$, air enters at the upper vent and exits at a colder temperature through the lower vent (Figure 13). $T_{air\ layer}$ is the mean of the temperature of the walls inside the ventilated air layer (T_{int}) and the temperature of the insulated panel. It should be noted that air can exit very hot (nearly 35 °C) from the air layer, and this air temperature (T_{uv}) was correctly estimated. The temperature difference between measured and calculated air temperatures at the upper vent equals 0.4 °C on average for this period.
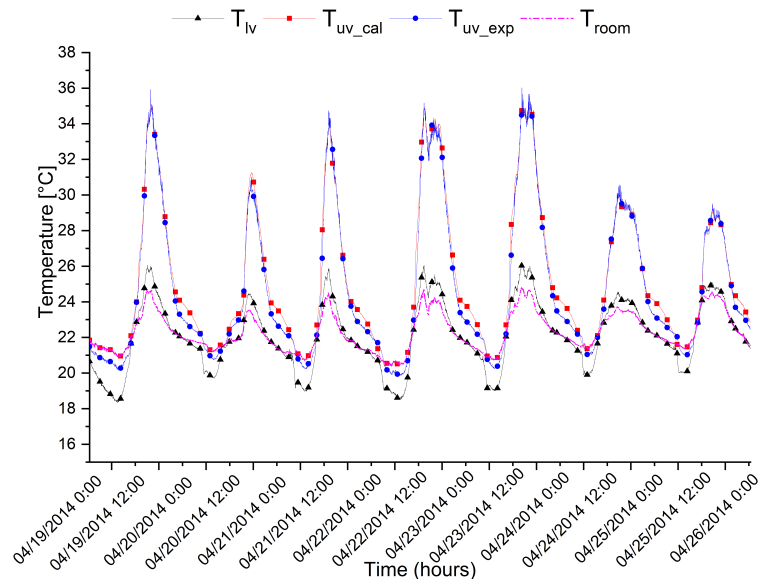

Figure 12. Comparison of air temperatures at the upper vent of the ventilated air layer (model results and experimentation). T_{lv} is the experimental air temperature at the lower vent of the ventilated air layer; T_{uv_cal} and T_{uv_exp} denote respectively the evolution in numerical and experimental air temperatures at the upper vent of the ventilated air layer; T_{room} is the room-temperature fluctuation.
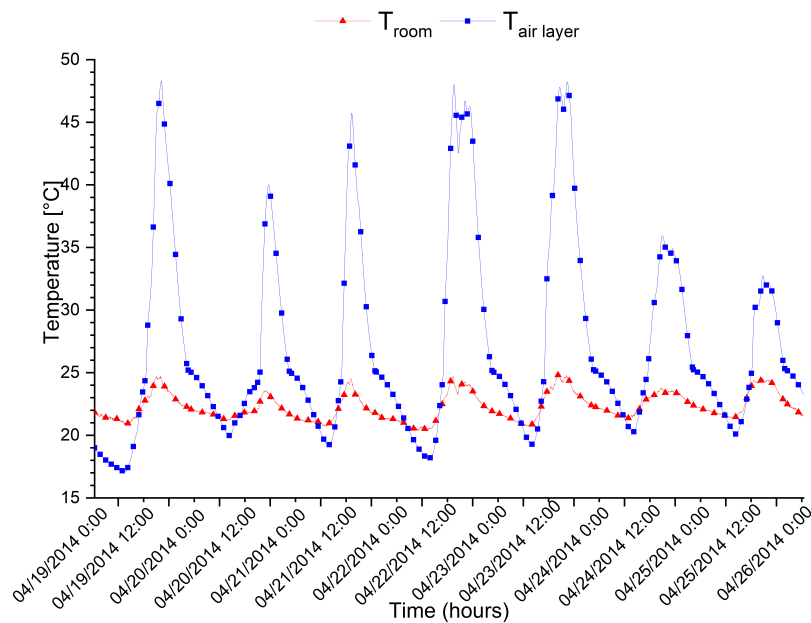

Figure 13. Evolution in the average air temperature inside the ventilated air layer ($T_{air\ layer}$) compared to the room-temperature fluctuation (T_{room}).

It can be observed that the air temperature curves at the upper vent (T_{uv_cal}, T_{uv_exp}) show very strong similarities between experimental measurements and numerical results. The comparison of heat fluxes exchanged and temperatures within the ventilated air layer serves to confirm the good level of agreement between behavioral modeling of a composite Trombe wall integrating PCM and experimentation. It is possible therefore to calculate the energy recovered through the energy balance of the solar wall over a given period (19–26 April 2014). This balance was calculated in the ventilated air layer using two methods validated in previous studies [22,24]. The first method is the energy balance due to the total head loss coefficient of air between the inlet and outlet of the ventilated air layer (Equation 32), while the second method is based on a direct heat flux measurement (Equation 33).

Figure 14 presents a comparison of the power released from the solar wall, as calculated by the numerical model and estimated from heat flux measurements over one week (19–26 April 2014). Small differences can be observed between the two curves; their comparison indicates that the power calculation compared to experimental measurements is indeed acceptable. The thermal energy supplied by the composite Trombe wall equals, over the period considered, 4.4 kWh/m^2 for the calculation and 4.7 kWh/m^2 for the estimation derived from fluxmeter measurements; the difference between the two methods is on the order of 6.3%.
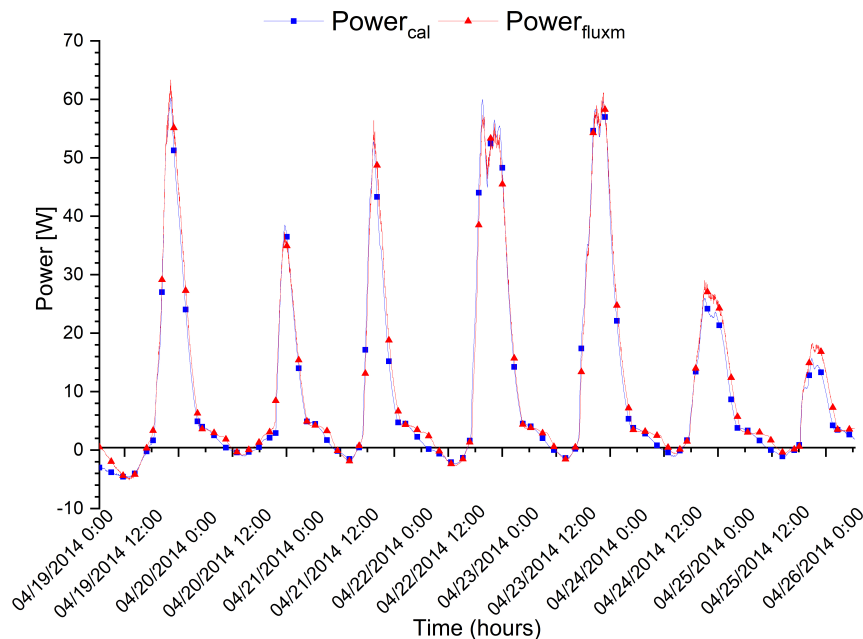

Figure 14. Comparison of the power released by the solar wall. Power$_{cal}$ denotes the power released according to calculation results, while Power$_{fluxm}$ is the power released according to fluxmeter measurements.

As regards the results listed in Table 3, the total accumulation of measured solar energy over this 7-day period (April 19-26, 2014) is equal to 21.4 kWh/m^2 (per m^2 of solar wall). Most recently, 35.8% of the total energy, i.e., 7.7 kWh/m^2, was absorbed by the storage wall at its external surface. The stored energy, which was released within a 3h 04 min time delay (calculation with cross-correlation function between ϕ_{ext} and ϕ_{int}) to the ventilated air layer is estimated at 4.7 kWh/m^2, which equals to 60.8% of the absorbed energy and 21.8% of the energy generated from the total incident solar flux on the vertical facade of the solar wall (as measured by the pyranometer).

As indicated above, the enthalpy method implemented in the composite solar wall model also provided accurate predictions for reproducing the thermal behavior of the latent heat and estimating the amount of energy released. One question worth asking is whether the latent heat storage is more or less efficient than sensible heat storage for the same volume. For the simulation of the composite

Trombe wall in the case of sensible heat storage, a model developed earlier and validated in previous studies [24] will be used; it was composed of conventional building materials (solid concrete blocks).

Both these models will now serve to compare the efficiency of each of these two types of solar wall by applying the meteorological data from Section 3.

Table 3. Comparison of thermal energy results from calculation and experimental methods.

	Symbol	Explanation	Unit	Value
Solar energy	E_{sol}	energy	kWh/m^2	21.4
Energy absorbed	E_{pcm,ext_cal}	energy	kWh/m^2	7.8
	E_{pcm,ext_exp}	energy	kWh/m^2	7.7
	-	variance	%	1.3
Solar release	E_{pcm,int_cal}	energy	kWh/m^2	5.1
	E_{pcm,int_exp}	energy	kWh/m^2	4.7
	-	variance	%	7.8

6. Comparing Performance of Composite Solar Walls with Sensible vs. Latent Heat Storage

To compare the energy efficiency of the storage type of composite solar wall, numerical simulations were carried out using the material characteristics identified in a previous work published in [69]. The two materials characterized are a cement mortar (CM) and a cement mortar containing 19% by weight of micro-encapsulated PCM (M+PCM). The PCM used is Micronal® PCM DS 5001 X, i.e., the same as that incorporated into the experimental solar wall studied herein. Previous works highlighted that the micro-encapsulated PCM incorporated into mortar allows for 41% more energy to be stored compared to cement mortar. The thermophysical parameters of these materials are reported in Table 4 below. These same materials were introduced into the composite Trombe wall model to run the simulations.

Table 4. Material properties.

Material	Mortar	PCM-M Solid State | Liquid State
Thermal Conductivity ($W.m^{-1}.K^{-1}$)	0.65	0.37
Heat Capacity ($J.kg^{-1}.K^{-1}$)	925	1255; 1238
Latent Heat ($J.kg^{-1}$)	—	19,520
Density ($kg.m^{-3}$)	2001	1248

The simulations were conducted with the meteorological data presented in Section 3 and used to validate the solar wall model in the previous section. To compare the two storage types, the temperature on both sides of the storage wall and the power released by the ventilated air layer are presented in Figures 15 and 16.

As regards the temperature on both sides of the storage wall (see Figure 15), no major differences exist, except before midnight when the storage wall energy released and temperature decrease. At these times, inflections in the $T_{ext,m+pcm}$ and $T_{int,m+pcm}$ curves can be detected. For the cement mortar + PCM storage wall, PCM solidifies and releases latent heat, in which case the storage wall remains warmer longer. As such, the cement mortar + PCM storage wall can release energy later, which helps avoid reverse thermocirculation (as highlighted in Figure 16 by negative powers for the cement mortar storage).

In considering the energy supplied by the two solar walls, the energy balance over the study period equals 4.5 kW/m^2 for the solar wall equipped with cement mortar storage and 3.9 kW/m^2 for the solar wall equipped with mortar + PCM storage. Surprisingly, the solar wall capable of storing more energy is not the more efficient. The possible reason for this finding is either a lower transfer rate or a different energy storage than initially thought. The first reason pertains to the fact that

thermal conductivity is almost 1.75 times lower for cement mortar with PCM. Furthermore, if the solar wall operating temperature range were to be examined, it would differ from that of the study cited [69]. In that previous study, the temperature range spanned 28 °C (between 11.4 °C and 39.4 °C), while the thermal capacity was 41% greater for the mortar integrating PCM. In this present case, the temperature range spans 45 °C (from 15 °C to 60 °C , in considering the average maximum temperatures); consequently, the difference is slightly higher, by 13%, in favor of the mortar + PCM. Hence, the higher thermal conductivity and lower total thermal capacity of storage without PCM produce a faster and greater energy release from the solar wall equipped with cement mortar storage and, therefore over the study period, improved energy efficiency.
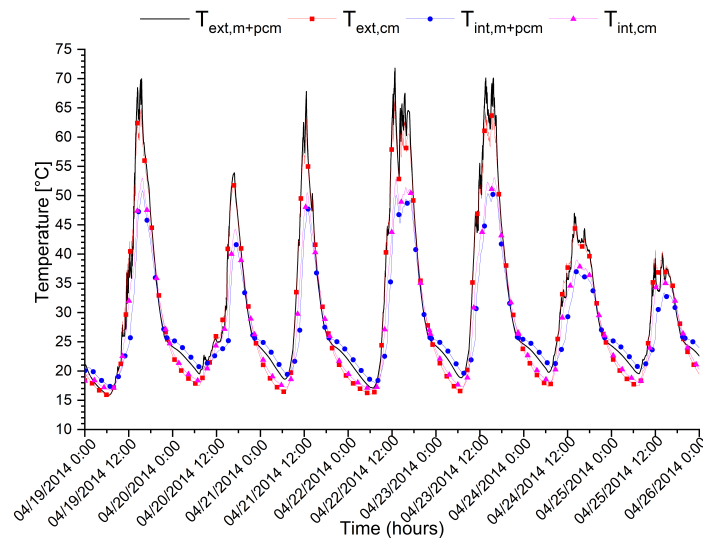

Figure 15. Comparison of temperature on both sides of the storage wall (cement mortar and mortar containing PCM). $T_{ext,m+pcm}$ and $T_{ext,cm}$ denote respectively the evolution in numerical temperatures on the exterior surface of the storage wall made from mortar containing PCM and that made from cement mortar; $T_{int,m+pcm}$ and $T_{int,cm}$ denote respectively the evolution in numerical temperatures on the interior surface of the storage wall made from mortar containing PCM and that made from cement mortar.
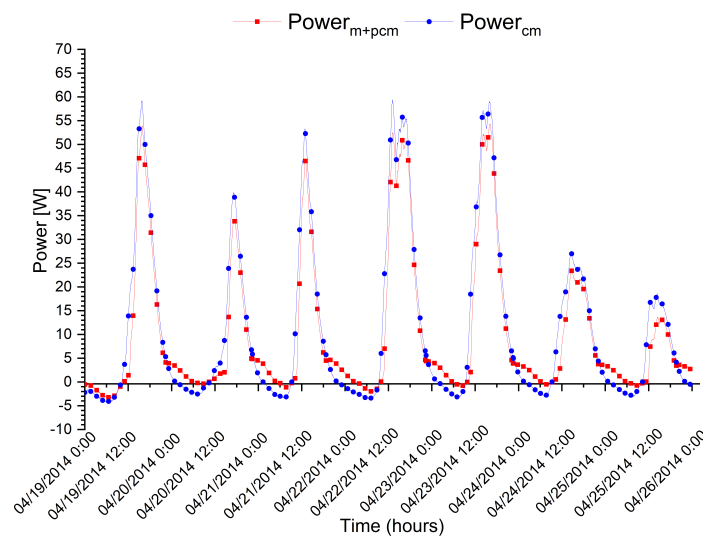

Figure 16. Comparison of the power released by the solar wall. $Power_{m+pcm}$ and $Power_{cm}$ denote respectively the evolution in the numerical results of power released from the solar wall integrating a storage wall containing PCM and that integrating a storage wall made from cement mortar.

7. Conclusions

The primary objective of this work was to present a numerical model for simulating the thermal behavior of a composite solar wall integrating a micro-encapsulated phase change material. As a secondary objective, this model was used to compare the thermal performance of two composite solar walls, one with sensible heat storage the other relying on latent heat storage.

The passive operations of the solar wall were first explained. This type of south-facing solar wall in the northern hemisphere is suitable for heating residential buildings during the cold weather season due to the time lag of solar gains.

A small-scale wall was built, instrumented and exposed to real weather conditions in order to validate the numerical model developed with the Dymola software, based on the open-source Modelica modeling language. The composite solar wall entails all three modes of heat transfer. To model these transfers, the basic elements from the software's "Building" library were assembled. A new element was created to model heat transfers from the storage wall containing the phase change material (melting and solidification). This additional element was based on the enthalpy method developed and validated in previous studies.

Validating the thermal behavior of the solar wall involves comparing measurements (heat flux, temperature, power released) to simulation results. This step demonstrated the model's good accuracy. The difference between experimental measurements and numerical results is less than 10% for both heat flow and energy released by the solar wall, i.e., on the order of 1 °C on the storage wall surfaces and less than 0.5 °C on the ventilated layer air temperature.

By measuring heat flux on the storage wall over a 7-day period, it was determined that the total stored energy from the external surface corresponds to 35.8% of the incident solar energy radiating the vertical facade. 60.8% of this energy is released into the room to be heated, which is equivalent to 21.8% of the incident solar energy. A cross-correlation function calculation between the heat fluxes measured on the two storage wall surfaces (ϕ_{ext} and ϕ_{int}) allowed evaluating the time delay between the incident solar flux and the energy released to the room at 3 h and 4 min for a 4-cm thick storage wall including micro-encapsulated PCM.

The study concluded with a comparison of the performance of a composite solar wall equipped with cement mortar storage (i.e., sensible heat storage) vs. the performance of the wall previously studied (latent heat storage). For purposes of this comparison, the numerical model developed and validated in the first step and the experimental meteorological data were used. It was shown that latent heat storage does not improve solar wall efficiency. The reasons cited for this finding were: a lower transfer rate due to less thermal conductivity for the latent heat storage, which stems from incorporating PCM into the cement mortar (thus lowering its density); and an operating temperature range of 45 °C , which is not beneficial to latent heat storage vs. sensible heat storage.

Nomenclature

Symbols:

A	area, m^2
A_{exch}	exchange surface, m^2
C	heat capacity, J/K
c	specific heat capacity, J/kg K
c_f	specific heat capacity of fluid, J/kg K
c_{solid}	specific heat capacity when PCM is in the solid state, J/kg K
c_{liquid}	specific heat capacity when PCM is in the liquid state, J/kg K
E	thermal energy, J
e	thickness, m
Gr	Grashof number
H	height, m
h	specific enthalpy, J/kg
h_c	convective heat transfer coefficient, W/m^2 K
h_{c1}	convective heat transfer coefficient in non-ventilated air layer, W/m^2 K
h_{c2}	convective heat transfer coefficient in ventilated air layer, W/m^2 K
h_r	radiative heat transfer coefficient, W/m^2 K
h_{r1}	radiant heat transfer coefficient between glazing and wall, W/m^2 K
h_{r2}	radiant heat transfer coefficient between wall and insulating panel, W/m^2 K
L_A	latent heat, J/kg
$\dot{m}$	air mass flow rate, kg/s
Nu	Nusselt number
P	power supplied by air layer, W
Pr	Prandtl number
Q_{sol}	solar radiation intensity, W/m^2
Ra	Rayleigh number
Re	Reynolds number
T	temperature, °C
t	time, s
V	velocity of wind, m/s
W	width, m

Greek symbols

α	absorptivity
β	dilatation coefficient at constant pressure, K^{-1}
δ_1	non ventilated air gap width, m
δ_2	ventilated air gap width, m
ε	emissivity
λ	thermal conductivity, W/m K
μ	dynamic viscosity of air, kg/m s
υ	kinematic viscosity of air, m^2/s
ξ_g	absorptivity of multi-reflection radiation intensity to glazing
ξ_w	global absorptivity of wall (including multi-reflection)
ρ	density, kg/m^3
σ	Stefan-Boltzmann constant, 5.67×10^{-8} W/m^2 K^4
τ	transmissivity
ϕ	heat flux, W

Subscripts

A	pure substance
amb	ambient
cal	calculation
env	environment
exp	experimentation
ext	exterior surface
f	fluid
f_1	fluid circulating in non-ventilated
f_2	fluid circulating in ventilated air layer
g	glazing
gro	ground
i	initial
ins	insulating
int	interior surface
lv	lower vent
M	melting
uv	upper vent
w	wall (storage wall)

Abbreviations

CM	cement mortar
M_PCM	composite material: mortar + PCM
PCM	phase change material
Q_cm	internal capacity of CM
Q_pcm	internal capacity of M_PCM

References

1. Buzzoni, L.; Dall'Olio, R.; Spiga, M. Energy analysis of a passive solar system. *Rev. Générale Therm.* **1998**, *37*, 411–416. [CrossRef]
2. Chan, H.Y.; Riffat, S.B.; Zhu, J. Review of passive solar heating and cooling technologies. *Renew. Sustain. Energy Rev.* **2010**, *14*, 781–789. [CrossRef]
3. Dabaieh, M.; Elbably, A. Ventilated Trombe wall as a passive solar heating and cooling retrofitting approach; a low-tech design for off-grid settlements in semi-arid climates. *Sol. Energy* **2015**, *122*, 820–833. [CrossRef]
4. Hassanain, A.A.; Hokam, E.M.; Mallick, T.K. Effect of solar storage wall on the passive solar heating constructions. *Energy Build.* **2011**, *43*, 737–747. [CrossRef]
5. Wang, D.; Liu, Y.; Jiang, J.; Liu, J. The Optimized Matching of Passive Solar Energy supply and Classroom Thermal Demand of Rural Primary and Secondary School in Northwest China. *Procedia Eng.* **2015**, *121*, 1089–1095. [CrossRef]
6. Castell, A.; Martorell, I.; Medrano, M.; Pérez, G.; Cabeza, L.F. Experimental study of using PCM in brick constructive solutions for passive cooling. *Energy Build.* **2010**, *42*, 534–540. [CrossRef]
7. Rekstad, J.; Meir, M.; Murtnes, E.; Dursun, A. A comparison of the energy consumption in two passive houses, one with a solar heating system and one with an air–water heat pump. *Energy Build.* **2015**, *96*, 149–161. [CrossRef]
8. Santamouris, M.; Argiriou, A.; Vallindras, M. Design and operation of a low energy consumption passive solar agricultural greenhouse. *Sol. Energy* **1994**, *52*, 371–378. [CrossRef]
9. Taleb, H.M. Using passive cooling strategies to improve thermal performance and reduce energy consumption of residential buildings in U.A.E. buildings. *Front. Archit. Res.* **2014**, *3*, 154–165. [CrossRef]
10. Tyagi, V.V.; Buddhi, D. PCM thermal storage in buildings: A state of art. *Renew. Sustain. Energy Rev.* **2007**, *11*, 1146–1166. [CrossRef]
11. Mazria, E. *Passive Solar Energy Book*; Rodale Press: Emmaus, PA, USA, 1979.
12. Trombe, F. Maisons solaires. *Techniques de l'ingenieur* **1974**, *3*, 375–382.
13. Smolec, W.; Thomas, A. Theoretical and experimental investigations of heat transfer in a trombe wall. *Energy Convers. Manag.* **1993**, *34*, 385–400. [CrossRef]

14. Utzinger, D.M.; Klein, S.A.; Mitchell, J.W. The effect of air flow rate in collector-storage walls. *Sol. Energy* **1980**, *25*, 511–519. [CrossRef]

15. Yedder, R.B.; Bilgen, E. Natural convection and conduction in Trombe wall systems. *Int. J. Heat Mass Transf.* **1991**, *34*, 1237–1248. [CrossRef]

16. Gracia, A.d.; Cabeza, L.F. Phase change materials and thermal energy storage for buildings. *Energy Build.* **2015**, *103*, 414–419. [CrossRef]

17. Fiorito, F. Trombe Walls for Lightweight Buildings in Temperate and Hot Climates. Exploring the Use of Phase-change Materials for Performances Improvement. *Energy Procedia* **2012**, *30*, 1110–1119. [CrossRef]

18. Ghoneim, A.A.; Klein, S.A.; Duffie, J.A. Analysis of collector-storage building walls using phase-change materials. *Sol. Energy* **1991**, *47*, 237–242. [CrossRef]

19. Sharma, A.; Tyagi, V.V.; Chen, C.R.; Buddhi, D. Review on thermal energy storage with phase change materials and applications. *Renew. Sustain. Energy Rev.* **2009**, *13*, 318–345. [CrossRef]

20. Stritih, U.; Novak, P. Solar heat storage wall for building ventilation. *Renew. Energy* **1996**, *8*, 268–271. [CrossRef]

21. Zhou, G.; Pang, M. Experimental investigations on thermal performance of phase change material—Trombe wall system enhanced by delta winglet vortex generators. *Energy* **2015**, *93*, 758–769. [CrossRef]

22. Leang, E.; Tittelein, P.; Zalewski, L.; Lassue, S. Numerical study of a composite Trombe solar wall integrating microencapsulated PCM. *Energy Procedia* **2017**, *122*, 1009–1014. [CrossRef]

23. Shen, J.; Lassue, S.; Zalewski, L.; Huang, D. Numerical study on thermal behavior of classical or composite Trombe solar walls. *Energy Build.* **2007**, *39*, 962–974. [CrossRef]

24. Zalewski, L.; Chantant, M.; Lassue, S.; Duthoit, B. Experimental thermal study of a solar wall of composite type. *Energy Build.* **1997**, *25*, 7–18. [CrossRef]

25. Zalewski, L.; Joulin, A.; Lassue, S.; Dutil, Y.; Rousse, D. Experimental study of small-scale solar wall integrating phase change material. *Sol. Energy* **2012**, *86*, 208–219. [CrossRef]

26. Zrikem, Z.; Bilgen, E. Theoretical study of a composite Trombe-Michel wall solar collector system. *Sol. Energy* **1987**, *39*, 409–419. [CrossRef]

27. Irshad, K.; Habib, K.; Thirumalaiswamy, N. Performance Evaluation of PV-trombe Wall for Sustainable Building Development. *Procedia CIRP* **2015**, *26*, 624–629. [CrossRef]

28. Irshad, K.; Habib, K.; Thirumalaiswamy, N. Energy and Cost Analysis of Photo Voltaic Trombe Wall System in Tropical Climate. *Energy Procedia* **2014**, *50*, 71–78. [CrossRef]

29. Jiang, B.; Ji, J.; Yi, H. The influence of PV coverage ratio on thermal and electrical performance of photovoltaic-Trombe wall. *Renew. Energy* **2008**, *33*, 2491–2498. [CrossRef]

30. Jie, J.; Hua, Y.; Gang, P.; Bin, J.; Wei, H. Study of PV-Trombe wall assisted with DC fan. *Build. Environ.* **2007**, *42*, 3529–3539. [CrossRef]

31. Jie, J.; Hua, Y.; Wei, H.; Gang, P.; Jianping, L.; Bin, J. Modeling of a novel Trombe wall with PV cells. *Build. Environ.* **2007**, *42*, 1544–1552. [CrossRef]

32. Jie, J.; Hua, Y.; Gang, P.; Jianping, L. Study of PV-Trombe wall installed in a fenestrated room with heat storage. *Appl. Therm. Eng.* **2007**, *27*, 1507–1515. [CrossRef]

33. Koyunbaba, B.K.; Yilmaz, Z.; Ulgen, K. An approach for energy modeling of a building integrated photovoltaic (BIPV) Trombe wall system. *Energy Build.* **2013**, *67*, 680–688. [CrossRef]

34. Koyunbaba, B.K.; Yilmaz, Z. The comparison of Trombe wall systems with single glass, double glass and PV panels. *Renew. Energy* **2012**, *45*, 111–118. [CrossRef]

35. Sun, W.; Ji, J.; Luo, C.; He, W. Performance of PV-Trombe wall in winter correlated with south façade design. *Appl. Energy* **2011**, *88*, 224–231. [CrossRef]

36. Taffesse, F.; Verma, A.; Singh, S.; Tiwari, G.N. Periodic modeling of semi-transparent photovoltaic thermal-trombe wall (SPVT-TW). *Sol. Energy* **2016**, *135*, 265–273. [CrossRef]

37. Saadatian, O.; Sopian, K.; Lim, C.H.; Asim, N.; Sulaiman, M.Y. Trombe walls: A review of opportunities and challenges in research and development. *Renew. Sustain. Energy Rev.* **2012**, *16*, 6340–6351. [CrossRef]

38. Gan, G. A parametric study of Trombe walls for passive cooling of buildings. *Energy Build.* **1998**, *27*, 37–43. [CrossRef]

39. Hu, Z.; He, W.; Ji, J.; Zhang, S. A review on the application of Trombe wall system in buildings. *Renew. Sustain. Energy Rev.* **2017**, *70*, 976–987. [CrossRef]

40. Stazi, F.; Mastrucci, A.; di Perna, C. The behaviour of solar walls in residential buildings with different insulation levels: An experimental and numerical study. *Energy Build.* **2012**, *47*, 217–229. [CrossRef]

41. Dutil, Y.; Rousse, D.; Lassue, S.; Zalewski, L.; Joulin, A.; Virgone, J.; Kuznik, F.; Johannes, K.; Dumas, J.P.; Bédécarrats, J.P.; et al. Modeling phase change materials behavior in building applications: Comments on material characterization and model validation. *Renew. Energy* **2014**, *61*, 132–135. [CrossRef]

42. Khudhair, A.M.; Farid, M.M. A review on energy conservation in building applications with thermal storage by latent heat using phase change materials. *Energy Convers. Manag.* **2004**, *45*, 263–275. [CrossRef]

43. Zalba, B.; Marin, J.M.; Cabeza, L.F.; Mehling, H. Review on thermal energy storage with phase change: materials, heat transfer analysis and applications. *Appl. Therm. Eng.* **2003**, *23*, 251–283. [CrossRef]

44. Swet, C. Phase change storage in passive solar architecture. *Proc. Annu. Meet. Am. Sect. Int. Sol. Energy Soc.* **1980**, *5*, 282–286.

45. Bourdeau, L. Utilisation d'un matériau à changement de phase dans un mur Trombe sans thermocirculation. *Rev. Phys. Appl.* **1982**, *17*, 633–642. [CrossRef]

46. Khalifa, A.J.N.; Abbas, E.F. A comparative performance study of some thermal storage materials used for solar space heating. *Energy Build.* **2009**, *41*, 407–415. [CrossRef]

47. Li, Y.; Liu, S. Experimental study on thermal performance of a solar chimney combined with PCM. *Appl. Energy* **2014**, *114*, 172–178. [CrossRef]

48. Zhou, Y.; Yu, C.W.F.; Zhang, G. Study on heat-transfer mechanism of wallboards containing active phase change material and parameter optimization with ventilation. *Appl. Therm. Eng.* **2018**, *144*, 1091–1108. [CrossRef]

49. Liu, X.; Zhou, Y.; Zhang, G. Numerical study on cooling performance of a ventilated Trombe wall with phase change materials. *Build. Simul.* **2018**, *11*, 677–694. [CrossRef]

50. Baetens, R.; De Coninck, R.; Jorissen, F.; Picard, D.; Helsen, L.; Saelens, D. Openideas-an open framework for integrated district energy simulations. In Proceedings of the 14th International Conference of IBPSA—Building Simulation, Hyderabad, India, 7–9 December 2015; pp. 347–354.

51. Wetter, M.; Bonvini, M.; Nouidui, T.S.; Tian, W.; Zuo, W. Modelica buildings library 2.0. In Proceedings of the 14th International Conference of IBPSA—Building Simulation, Hyderabad, India, 7–9 December 2015; pp. 387–394.

52. Zhou, Y.; Zheng, S.; Zhang, G. Study on the energy performance enhancement of a new PCMs integrated hybrid system with the active cooling and hybrid ventilations. *Energy* **2019**, *179*, 111–128. [CrossRef]

53. Zhou, Y.; Zheng, S.; Zhang, G. Machine-learning based study on the on-site renewable electrical performance of an optimal hybrid PCMs integrated renewable system with high-level parameters' uncertainties. *Renew. Energy* **2019**. [CrossRef]

54. Zhou, Y.; Zheng, S.; Zhang, G. Artificial neural network based multivariable optimization of a hybrid system integrated with phase change materials, active cooling and hybrid ventilations. *Energy Convers. Manag.* **2019**, *197*, 111859. [CrossRef]

55. Tang, L.; Zhou, Y.; Zheng, S.; Zhang, G. Exergy-based optimisation of a phase change materials integrated hybrid renewable system for active cooling applications using supervised machine learning method. *Sol. Energy* **2020**, *195*, 514–526. [CrossRef]

56. Liu, X.; Zhou, Y.; Li, C.Q.; Lin, Y.; Yang, W.; Zhang, G. Optimization of a New Phase Change Material Integrated Photovoltaic/Thermal Panel with The Active Cooling Technique Using Taguchi Method. *Energies* **2019**, *12*, 1022. [CrossRef]

57. Zalewski, L. Etude Thermique Expérimentale et Simulation Numérique d'un mur Solaire Composite. Optimisation des Performances énergétiques. Ph.D. Thesis, Univ. Artois, Arras, France, 1996.

58. Leclercq, D.; Thery, P. Apparatus for simultaneous temperature and heat-flow measurements under transient conditions. *Rev. Sci. Instrum.* **1983**, *54*, 374–380. [CrossRef]

59. Cherif, Y.; Joulin, A.; Zalewski, L.; Lassue, S. Superficial heat transfer by forced convection and radiation in a horizontal channel. *Int. J. Therm. Sci.* **2009**, *48*, 1696–1706. [CrossRef]

60. Sparrow, E.M.; Ramsey, J.W.; Mass, E.A. Effect of Finite Width on Heat Transfer and Fluid Flow about an Inclined Rectangular Plate. *J. Heat Transf.* **1979**, *101*, 199–204. [CrossRef]

61. Buchberg, H.; Catton, I.; Edwards, D.K. Natural Convection in Enclosed Spaces—A Review of Application to Solar Energy Collection. *J. Heat Transf.* **1976**, *98*, 182–188. [CrossRef]

62. Hollands, K.G.T.; Unny, T.E.; Raithby, G.D.; Konicek, L. Free Convective Heat Transfer Across Inclined Air Layers. *J. Heat Transf.* **1976**, *98*, 189–193. [CrossRef]

63. Franquet, E.; Gibout, S.; Tittelein, P.; Zalewski, L.; Dumas, J.P. Experimental and theoretical analysis of a cement mortar containing microencapsulated PCM. *Appl. Therm. Eng.* **2014**, *73*, 32–40. [CrossRef]

64. Tittelein, P.; Gibout, S.; Franquet, E.; Zalewski, L.; Defer, D. Identification of Thermal Properties and Thermodynamic Model for a Cement Mortar Containing PCM by Using Inverse Method. *Energy Procedia* **2015**, *78*, 1696–1701. [CrossRef]

65. Zalewski, L.; Franquet, E.; Gibout, S.; Tittelein, P.; Defer, D. Efficient Characterization of Macroscopic Composite Cement Mortars with Various Contents of Phase Change Material. *Appl. Sci.* **2019**, *9*, 1104. [CrossRef]

66. Tittelein, P.; Gibout, S.; Franquet, E.; Johannes, K.; Zalewski, L.; Kuznik, F.; Dumas, J.P.; Lassue, S.; Bédécarrats, J.P.; David, D. Simulation of the thermal and energy behaviour of a composite material containing encapsulated-PCM: Influence of the thermodynamical modelling. *Appl. Energy* **2015**, *140*, 269–274. [CrossRef]

67. Churchill, S.W.; Chu, H.H.S. Correlating equations for laminar and turbulent free convection from a vertical plate. *Int. J. Heat Mass Transf.* **1975**, *18*, 1323–1329. [CrossRef]

68. McAdams, W.H. *Transmission de la Chaleur*; Dunod: Paris, France, 1961.

69. Joulin, A.; Zalewski, L.; Lassue, S.; Naji, H. Experimental investigation of thermal characteristics of a mortar with or without a micro-encapsulated phase change material. *Appl. Therm. Eng.* **2014**, *66*, 171–180. [CrossRef]